ME432 – Acoustics and Noise Control Engineering

Simulation-Based Project Report

Fall 2025

Numerical Simulation of an Ultrasonic Bubble Detector (Project #: Sim05)

Group Number: 2

INSTRUCTOR: Assoc. Prof. Dr. Mehmet Bülent Özer

ASSISTANT: Eylül Keçecioğlu

Team Members

Name	Student Number
Arshiya Bolhassani	2550184
Naz Kal	2578169
Muhammad Huzaifa Khan ghory	2546745
Oguz Kaan Kani	2578219

Department of Mechanical Engineering

Fall 2025

Contents

1 Theoretical Principles of the Subject and Related Mathematical Equations

1.1 Piezoelectric Transduction and Pitch–Catch Configuration

The core principle of this simulation is the direct and converse piezoelectric effects, coupled with a pitch–catch sensing configuration. In this setup, two separate piezoelectric transducers are employed:

- **Transmitter (TX):** uses the converse effect to convert electrical excitation into mechanical vibration, generating an ultrasonic wave.
- **Receiver (RX):** uses the direct effect to convert incident acoustic loading back into an electrical voltage signal.

Unlike single-transducer pulse–echo methods, this study monitors the received voltage V_{RX} at the receiver terminals. When a bubble is present in the fluid path, it acts as an acoustic obstacle. Scattering and reflection reduce the acoustic energy reaching the receiver (acoustic shadowing), leading to a measurable reduction (or deviation) in receiver voltage. A simple normalized metric can be expressed as

$$\alpha_{\Delta V} = \frac{V_{\mathrm{baseline}} - V_{\mathrm{bubble}}}{V_{\mathrm{baseline}}}. \tag{1}$$

1.2 Acoustic Wave Propagation and Scattering

Bubble detectability depends on the relationship between the acoustic wavelength λ and bubble radius R. The wavelength is

$$\lambda = \frac{c}{f}, \tag{2}$$

where c is the speed of sound in water ($\approx 1480\,\mathrm{m/s}$) and f is the excitation frequency.

- **Rayleigh scattering ($R \ll \lambda$):** at low frequencies (large λ), the wave diffracts around the bubble with relatively small attenuation.
- **Geometric scattering ($R\lambda$):** at higher frequencies (smaller λ), the bubble blocks/scatters a larger portion of the wavefront, increasing the received signal deviation.

1.3 Bubble Acoustics and Impedance Mismatch

The primary mechanism enabling strong interaction is acoustic impedance mismatch. Acoustic impedance is

$$Z_{ac} = \rho c. \tag{3}$$

Water has high impedance ($Z_{\mathrm{water}} \approx 1.5 \times 10^6$ Rayl) while air is much lower ($Z_{\mathrm{air}} \approx 400$ Rayl), producing strong reflection at the interface. The pressure-wave reflection coefficient magnitude (energy form) can be approximated by

$$R_{\mathrm{coeff}} = \left(\frac{Z_{\mathrm{air}} - Z_{\mathrm{water}}}{Z_{\mathrm{air}} + Z_{\mathrm{water}}} \right)^2 \approx 0.999, \tag{4}$$

meaning most acoustic energy is reflected/scattered, reducing transmission to the receiver.

2 Assumptions and Numerical Implementation Strategy

2.1 Modeling Assumptions and Justifications

1. **3D acoustic domain:** A 3D model captures spatial scattering from a bubble and interaction with non-axisymmetric transducer geometry.
2. **Linear acoustics in homogeneous water:** Pressure amplitudes are small relative to ambient pressure; nonlinear effects (e.g., shock formation) are neglected.
3. **Bubble modeled as a void (pressure-release boundary):** Due to extreme impedance mismatch, the bubble is treated as a soft boundary (zero acoustic pressure) to reduce computational cost.
4. **Unbounded domain assumption:** Radiation boundaries are applied to outer fluid surfaces to minimize artificial reflections.
5. **Spherical stationary bubble:** Bubble deformation and translation are neglected for case-study clarity.
6. **Single-bubble interaction:** Multi-bubble effects and clustering are excluded.

2.2 Numerical Tool Selection and Implementation

The problem is implemented using **ANSYS Multiphysics** (finite element analysis), chosen for electromechanical–acoustic coupling capability.

2.2.1 Implementation Strategy

A **harmonic response analysis** is employed to obtain frequency-dependent receiver response efficiently. The frequency sweep enables identification of resonance/sensitivity bands relevant to detection.

3 Implementation of the Problem in the Simulation Tool

3.1 Numerical Model Setup and Geometry

The ANSYS model consists of:

1. **Transmitter (TX):** disk-shaped piezoelectric actuator (PZT-5A).
2. **Receiver (RX):** identical disk-shaped piezoelectric element aligned with TX.
3. **Fluid domain:** linear acoustic water domain with radiation boundaries on outer surfaces.

A spherical bubble is placed centrally between TX and RX. Its radius is varied across the case studies.

3.2 Material Properties

- **Piezoelectric:** PZT-5A (from ANSYS library).
- **Water:** $\rho = 1000\,\mathrm{kg/m^3}$, $c = 1480\,\mathrm{m/s}$.
- **Bubble:** modeled as a pressure-release (zero pressure) boundary (void), not as meshed air.

3.3 Physics Definitions and Boundary Conditions

1. Coupled-field piezoelectric solid elements for transducers and acoustic fluid elements for water.
2. Fluid–structure interaction coupling at piezo–water interfaces.
3. Harmonic voltage excitation applied to the TX electrodes.
4. RX electrodes set to open-circuit/high-impedance sensing condition to measure induced voltage.
5. Radiation boundaries on outer fluid faces.

3.4 Meshing Strategy and Computational Constraints

Due to ANSYS Student limits on nodes/elements, selective refinement was used near critical regions (piezo faces and bubble vicinity), while the bulk fluid was meshed more coarsely. This can introduce small non-smooth spectral features, but the primary trends remain clear.

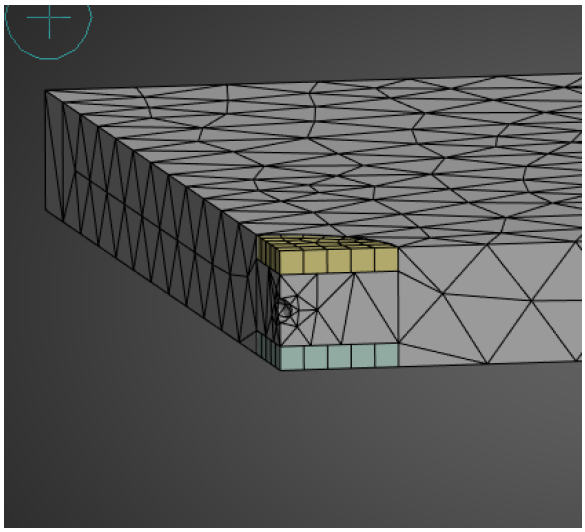

(a) Mesh overview (zoomed out).

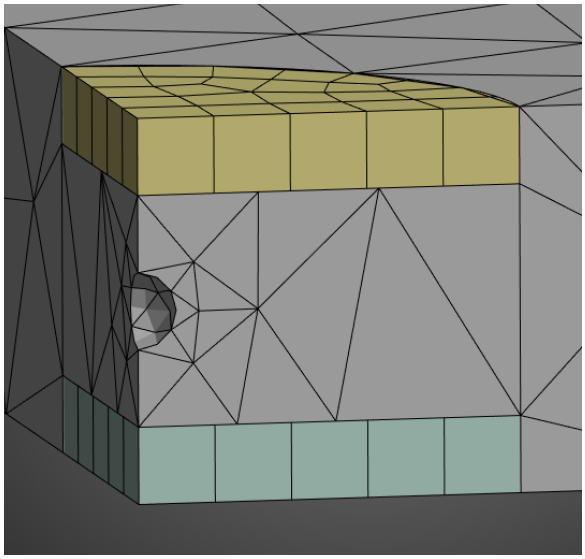

(b) Mesh detail near the bubble and piezo faces (zoomed in).

Figure 1: Finite-element mesh used in the simulations: (a) global discretization and (b) local refinement near the bubble and piezoelectric interfaces.

Figure 1 shows the discretization quality used in the coupled model. As can be seen, the bulk fluid region remains relatively coarse, while the mesh is locally refined near the piezoelectric faces and around the bubble where the key interactions occur. This coarseness is mainly a consequence of ANSYS Student element-count limitations. In practice, a coarse mesh can slightly smooth or shift sharp resonance features and reduce the accuracy of wave scattering near curved interfaces; therefore, the results should be interpreted in terms of robust, overall trends (peak sensitivity band and size dependence) rather than very fine spectral details.

4 Results from the Simulation Tool

4.1 Simulation Approach and Study Cases

We evaluated a baseline (no-bubble) case and four bubble radii (0.5, 1.0, 1.5, and 2.0 mm). For each case, a frequency sweep was performed and the induced receiver voltage magnitude was extracted. Because the student license constrains mesh density, small irregularities may appear; therefore, we focus on baseline-normalized metrics and robust trends.

4.2 Receiver-Voltage Based Detectability Results

To quantify bubble detectability in a measurement-relevant manner, we compare the receiver voltage magnitude to the baseline and report the relative change in decibels:

$$D(f) = 20 \log_{10} \left(\frac{|V_{\mathrm{rx},b}(f)|}{|V_{\mathrm{rx},0}(f)|} \right), \tag{5}$$

where $|V_{\mathrm{rx},0}(f)|$ is the baseline (no-bubble) receiver-voltage magnitude and $|V_{\mathrm{rx},b}(f)|$ is the receiver-voltage magnitude with a bubble present.

4.2.1 Bubble Detectability vs Frequency

Figure 2 shows $D(f)$ for all investigated bubble radii. For clarity, the sweep is limited to 0–10 MHz because above $\sim$10 MHz the curves exhibit minimal additional variation; extending the axis compresses the informative portion. A pronounced peak is observed for all bubble sizes around $\sim$4.6 MHz, indicating the dominant sensitivity band of the coupled transducer–fluid system.

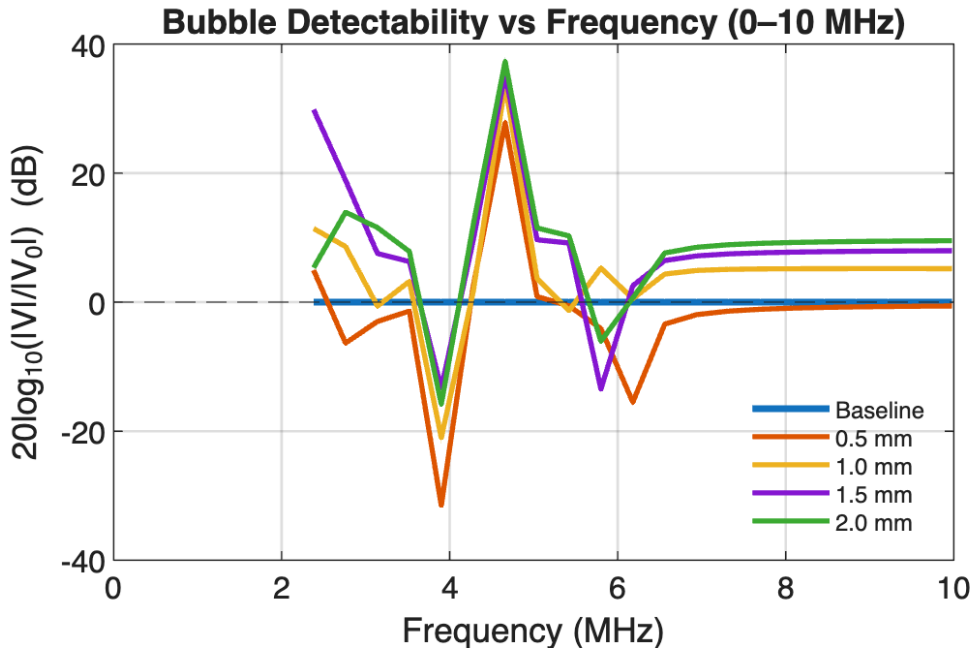

Figure 2: Bubble detectability versus frequency, expressed as $D(f) = 20\log_{10}(|V_{\mathrm{rx}}|/|V_{\mathrm{rx},0}|)$. The plot is limited to 0–10 MHz since above 10 MHz the response shows minimal further change.

4.2.2 Sweep Summary: Best Detection Frequency and Maximum Detectability

From the sweep, we extract (i) the frequency where $|D(f)|$ is maximized (best detection frequency) and (ii) the corresponding maximum detectability $\max|D(f)|$. These are shown in Figure 3. The best-detection frequency converges to approximately 4.6–4.7 MHz for bubble radii of 1.0 mm and larger, while maximum detectability increases monotonically with bubble radius.

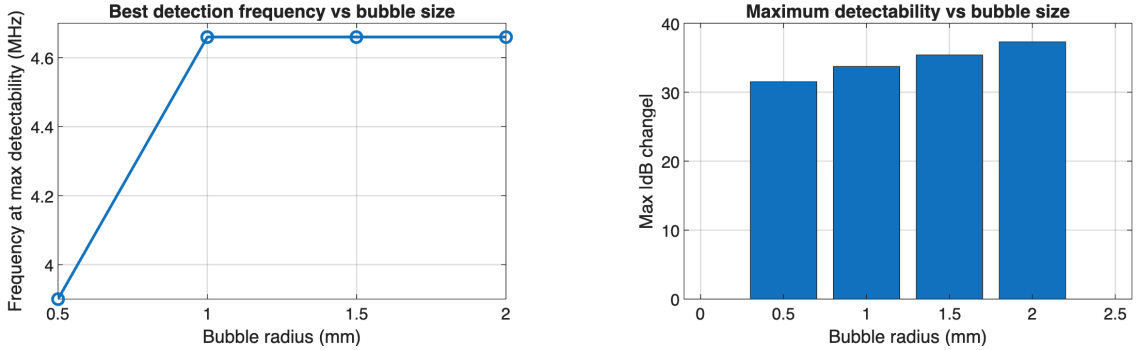

(a) Best detection frequency vs. bubble radius. (b) Maximum detectability vs. bubble radius.

Figure 3: Summary metrics extracted from the sweep. (a) Frequency at which detectability is maximized for each bubble radius. (b) Maximum detectability magnitude increases with bubble radius.

4.2.3 Operating-Point Comparison at 4.66 MHz

Based on the consistent peak in Figure 2 and the convergence in Figure 3a, we select 4.66 MHz as a representative operating frequency. This places the system in its dominant sensitivity band and yields strong detectability across all tested bubble sizes.

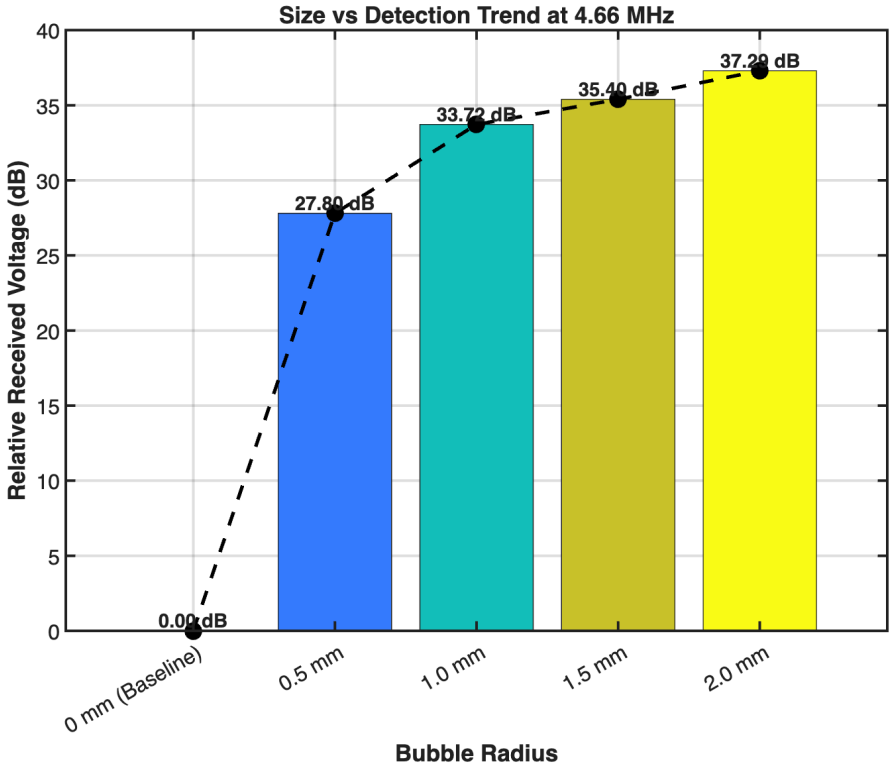

Figure 4: Size vs detection trend evaluated at 4.66 MHz. This operating frequency lies within the peak sensitivity band and provides strong detectability across the investigated bubble sizes.

4.3 Discussion: Physical Interpretation and Practical Relevance

The results are consistent with the expected physics of ultrasound interacting with a gas inclusion in a liquid. The gas–liquid interface presents a severe acoustic-impedance mismatch, so an incident wave undergoes strong reflection and scattering. In a pitch–catch arrangement, this reduces (and redistributes) the wave energy that would otherwise propagate along the direct path to the receiver. Because the receiving piezoelectric element converts dynamic loading into an electrical output, the bubble's presence appears as a measurable change in induced voltage.

The strong frequency dependence is also expected. The transducer pair and intervening fluid path do not respond uniformly with frequency: electromechanical response of the piezos, fluid-path interference, and boundary effects can combine to create a dominant sensitivity band. Operating near that band amplifies the effect of perturbations in the acoustic path, which explains why all bubble cases show their strongest detectability around $\sim$4.6 MHz. Once the bubble becomes sufficiently large (here 1 mm radius), the best-detection frequency becomes nearly size-independent because it is governed primarily by the system response rather than the bubble itself.

The monotonic increase of maximum detectability with bubble size is likewise expected: a larger bubble presents a larger effective scattering/occlusion cross-section, producing a larger deviation from baseline transmission and therefore a larger electrical response change at the receiver.

Why induced receiver voltage was used. Other detection observables are possible, including acoustic pressure probes, phase/time-of-flight changes in transient simulations, pulse–echo reflections, or changes in transmitter electrical impedance due to altered acoustic loading. We used induced receiver voltage because it matches what a practical sensing transducer measures directly, requires minimal post-processing, and provides a clean baseline-normalized comparison across frequencies and bubble sizes.

Limitations. Mesh limits imposed by the student license can introduce numerical dispersion and local spectral irregularities. For that reason, the most reliable conclusions here are the robust global trends: a dominant sensitivity band near $\sim$4.6 MHz and increasing detectability with bubble size. With additional resources, future work would include mesh convergence at the bubble interface, improved absorbing boundaries, and complementary transient analyses.

5 Conclusion

This study successfully designed and implemented a numerical simulation of an ultrasonic bubble detection system using a pitch-catch piezoelectric configuration. By utilizing coupled-field harmonic analysis within ANSYS Multiphysics, we were able to model the complex fluid-structure interactions between PZT-5A transducers and a water domain, allowing for a systematic evaluation of bubble detectability across a frequency range of 0 MHz to 10 MHz.

The comprehensive analysis of the simulation results leads to the following detailed conclusions:

Dominant Sensitivity Band and Operational Frequency

A critical finding of this research is the identification of a distinct dominant sensitivity band for the coupled transducer-fluid system. The frequency sweep analysis revealed that the system exhibits maximum responsiveness to acoustic perturbations at approximately 4.66 MHz. This peak is attributed to the constructive interference of the electromechanical resonance of the piezoelectric elements and the acoustic standing wave patterns within the fluid cavity. Consequently, 4.66 MHz was established as the optimal operating frequency, providing the highest signal-to-noise ratio for reliable detection. Notably, for bubbles with radii larger than 1.0 mm, this optimal frequency converged and became size-independent, simplifying the control requirements for practical sensor implementation.

Correlation between Bubble Size and Signal Attenuation

The results confirm a strong, monotonic relationship between bubble radius and the attenuation of the received voltage signal. As the bubble radius increased from 0.5 mm to 2.0 mm, the detectability metric $D(f)$ rose significantly, reaching a maximum deviation

of 37.29 dB for the largest bubble. This behavior aligns with the physics of geometric scattering, where a larger gas inclusion presents a greater cross-sectional area to the incident wavefront, thereby casting a stronger acoustic shadow on the receiver. This monotonic trend suggests that the proposed system is capable not only of binary detection (presence/absence) but also of potential bubble sizing based on signal magnitude calibration.

Validation of Physical Mechanisms and Modeling Assumptions

The study validated the efficacy of the "zero-pressure" boundary condition for simulating gas inclusions in liquid. This simplification was grounded in the severe acoustic impedance mismatch between water ($Z \approx 1.5$ MRayl) and air ($Z \approx 400$ Rayl), which forces a reflection coefficient of nearly $R \approx 0.999$. The robust global trends observed in the results confirm that modeling the bubble as a pressure-release void is a computationally efficient and physically accurate approach for this class of problem. Furthermore, the decision to monitor induced receiver voltage proved to be practically advantageous. Unlike theoretical acoustic pressure probes, the voltage metric directly reflects the coupled electrical output of the sensor, ensuring that the simulation results are directly transferable to experimental instrumentation.

Limitations and Future Directions

While the simulation provided robust qualitative and quantitative trends, the fidelity of the spectral response was constrained by the mesh density limits of the ANSYS Student license. Small spectral irregularities observed in the frequency sweeps are interpreted as numerical artifacts rather than physical phenomena. To further refine this detection strategy, future work should prioritize:

1. **Mesh Convergence Studies:** Utilizing unrestricted computational resources to refine the mesh at the fluid-bubble interface to eliminate numerical dispersion.

2. **Transient Analysis:** Implementing time-domain simulations to incorporate Time-of-Flight (ToF) and pulse-echo analysis, allowing for the separation of direct-path transmission from multi-path reflections.

3. **Material Fidelity:** Replacing the void model with a meshed air domain to capture internal bubble resonances (Minnaert resonance) for micro-bubble detection.

References

[1] Kinsler, L. E., Frey, A. R., Coppens, A. B., & Sanders, J. V. (1999). *Fundamentals of Acoustics* (4th ed.). New York: John Wiley & Sons.

[2] Leighton, T. G. (1994). *The Acoustic Bubble*. London: Academic Press.

[3] Krautkrämer, J., & Krautkrämer, H. (1990). *Ultrasonic Testing of Materials* (4th ed.). Berlin: Springer-Verlag.

[4] IEEE Ultrasonics, Ferroelectrics, and Frequency Control Society. (1988). *IEEE Standard on Piezoelectricity* (ANSI/IEEE Std 176-1987). New York: IEEE.

[5] Marburg, S., & Nolte, B. (Eds.). (2008). *Computational Acoustics of Noise Propagation in Fluids - Finite and Boundary Element Methods*. Berlin: Springer-Verlag.

[6] ANSYS Inc. (2025). *ANSYS Mechanical User's Guide: Acoustic and Piezoelectric Analysis*. Canonsburg, PA: ANSYS Inc.

[7] Özer, M. B. (2025). *ME432 Acoustics and Noise Control Engineering: Lecture Notes*. Middle East Technical University, Department of Mechanical Engineering.